

# Spin evolution modeling for a newly-formed white dwarf resulting from binary white dwarf merger

Yanchang Cheng,<sup>1\*</sup> and Jumpei Takata,<sup>1†</sup>

<sup>1</sup>*Department of Astronomy, School of Physics, Huazhong University of Science and Technology, Wuhan, Hubei 430074, China*

Accepted XXX. Received YYY; in original form ZZZ

## ABSTRACT

Merger of two white dwarfs (WDs) has been proposed to form an isolated WD having high magnetization and rapid rotation. We study the influence of the magnetohydrodynamic (MHD) wind on spin evolution of the newly-formed merger product. We consider the scenario that the merger product appears as a giant-star-like object with a radius of  $> 10^{10}$  cm and a luminosity of the order of an Eddington value. We solve a structure of the merger product under the hydrostatic equilibrium and identify the position of the slow-point in the hot envelope. It is found that if such a giant-star-like object is spinning with an angular speed of the order of the Keplerian value, the MHD wind can be produced. The mass-loss rate is estimated to be of the order of  $\sim 10^{20-21}$  g s<sup>-1</sup>, and the timescale of the spin down is  $\sim 10 - 10^3$  years, which depends on stellar magnetic field. We discuss that the final angular momentum when the MHD wind is terminated is related to the magnetic flux and initial radiation luminosity of the merger product. We apply our model to three specific magnetic WD sources ZTF J190132.9+145808.7, SDSS J221141.8+113604.4, and PG 1031+234 by assuming that those WDs were as a result of the merger product. We argue that the current periods of ZTF J190132.9+145808.7 and PG 1031+234 that are strongly magnetized WDs are related to the initial luminosity at the giant phase. For SDSS J221141.8+113604.4, which is mildly magnetized WD, its angular momentum was almost determined when the spin-down timescale due to MHD wind is comparable to the cooling timescale in the giant phase.

**Key words:** stars: winds, outflows – stars: evolution – white dwarfs

## 1 INTRODUCTION

White dwarf (hereafter WD) is the end product of a main-sequence star (hereafter MS) with a mass less than  $\sim 8 M_{\odot}$  and it is the most common endpoint of the stellar evolution; for example, Korol et al. (2020) estimate that total number of the WD in the Milky Way is estimated to be  $\sim 3 \times 10^9$ . A WD can be produced not only as a result of the single stellar evolution but also as a result of a merger of two stars in the binary system (Badenes & Maoz 2012; Shen et al. 2012; Temmink et al. 2020). It has been estimated that about 10–30% of the single WDs in the Milky Way are the products of the binary merger (Badenes & Maoz 2012; Maoz & Hallakoun 2017; Cheng et al. 2020; Temmink et al. 2020). Recent *Gaia* observation is drastically increasing the population of known WDs (Tremblay et al. 2024, and reference therein), and has also collected evidences of the WD produced by the binary merger process (Cheng et al. 2019, 2020; Kilic et al. 2023). For example, Cheng et al. (2020) find that the distribution of the transverse velocity of the massive WD with  $(0.8 - 1.3) M_{\odot}$  deviates significantly from the case predicted by the WD produced via the single stellar evolution and they suggest that the additional production process of the massive WD is required. Temmink et al. (2020) use the binary evolution synthesis code for the production of the WD through the various type binary merger

(MS+MS binary, MS+WD binary, WD+WD binary, etc), and demonstrate that the WD+WD binary merger (hereafter DWD merger) is the dominant process to create the massive WDs ( $> 0.9 M_{\odot}$ ). It has also been proposed that the DWD merger produces a highly magnetized WD (Wickramasinghe & Ferrario 2000; García-Berro et al. 2012; Ji et al. 2013; Hernandez et al. 2024). In particular, the recent observations have revealed a number of *isolated* massive, fast-spinning and high-field WDs that were probably produced through the WD+WD binary channel. SDSS J221141.8+113604.4 (hereafter J2211+1136) is one of the fastest spinning isolated WD with a spin period of  $P_{WD} \sim 70.32$  s, a stellar mass of  $M_{WD} \sim 1.27 M_{\odot}$  and a dipole field strength of  $B_{WD} \sim 1.5 \times 10^7$  G (Kilic et al. 2021b). ZTF J190132.9+145808.7 (hereafter J1901+1458) has a spin period of  $P_{WD} \sim 416.4$  s, a mass of  $M_{WD} \sim (1.327 - 1.365) M_{\odot}$  and a magnetic field of  $B_{WD} \sim (6 - 9) \times 10^8$  G (Caiazzo et al. 2021). WD J005311 is the WD identified in a mid-infrared nebula that is thought to be a result of a DWD merger event (Gvaramadze et al. 2019). This is because its effective temperature (around  $2 \times 10^5$  K) and the feature of deficiency of hydrogen and helium from the central star and nebula agree with the evolution of a DWD merger product predicted by Schwab et al. (2016). Kashiyama et al. (2019) propose that the mid-infrared nebula around the WD J005311 is powered by a fast-spinning and high-field WD ( $P_{WD} \sim 2 - 5$  s and  $B_{WD} \sim (2 - 5) \times 10^7$  G). Such a fast-spinning and highly magnetized WD may accelerate the charged particles in the magnetosphere and produce non-thermal radiation, as the X-ray emis-

\* E-mail: chengyc@hust.edu.cn

† E-mail: takata@hust.edu.cn

sion from J1901+1458 indicates (Bamba et al. 2024). These rapidly spinning magnetized WD also gives a hint of the origin of classical magnetic WD with a longer spin period and a smaller mass, such as PG 1031+234 ( $M_{WD} \sim 0.96 M_{\odot}$ ,  $P_{WD} \sim 212$  min and  $B_{WD} \sim (2 - 10) \times 10^8$  G) (Schmidt et al. 1986; Brinkworth et al. 2007; Gentile Fusillo et al. 2021). If these magnetic WDs are product of the DWD merger, a unified picture of the spin-evolution after the merger will be necessary to understand the difference in the spin periods among the magnetic WDs.

In this study, we assume that the DWD merger events produce the isolated magnetized WDs. It has been suggested that the merger product appears with a luminosity of the order of Eddington value,  $L_E \sim 3.2 \times 10^4 L_{\odot} (M_{WD}/M_{\odot})$  (Wu et al. 2022). The cooling age of the WD radiating luminosity of  $L_{WD}$  may be estimated from (Koester & Chanugam 1992),

$$\tau_{cool} \sim \frac{10^8}{A} \left( \frac{M_{WD}}{M_{\odot}} \right)^{0.609} \left( \frac{L_{WD}}{L_{\odot}} \right)^{-0.609} \text{ years}, \quad (1)$$

where  $A$  is the atomic mass number. Assuming CO core ( $A \sim 12$ ), the current cooling age is estimated to be  $\tau_{cool} \sim 3$  Gyr for J2211+1136 (Kilic et al. 2021a),  $\tau_{cool} \sim 0.075$  Gyr for J1901+1458 with the observed luminosity of  $L \sim 0.03 L_{\odot}$  (Caiazzo et al. 2021), while  $\tau_{cool} \sim 0.1$  Gyr for PG 1031+234 with  $L \sim 0.01 L_{\odot}$  (Gentile Fusillo et al. 2021). On the other hand, by assuming that the measured magnetic field,  $B_{WD}$ , represents the dipole magnetic field of the WD, we may estimate the spin-down timescale due to the dipole radiation as

$$\begin{aligned} \tau_{sd} &= \frac{3}{(2\pi)^2} \frac{c^3 P_{WD}^2 I_{WD}}{R_{WD}^6 B_s^2 \sin^2 \chi} \\ &\sim 0.5 \text{ Gyr} \left( \frac{P_{WD}}{100 \text{ s}} \right)^2 \left( \frac{B_{WD}}{10^8 \text{ G}} \right)^{-2} \\ &\quad \left( \frac{R_{WD}}{5 \cdot 10^8 \text{ cm}} \right)^{-6} \left( \frac{I_{WD}}{10^{50} \text{ g cm}^2} \right) \sin^{-2} \chi, \end{aligned} \quad (2)$$

where  $\chi$  is the inclination angle of the magnetic axis,  $R_{WD}$  is the radius of the WD, and  $I_{WD}$  is the moment of inertia. We can see that with the estimated mass  $M_{WD} \sim 1.3 M_{\odot}$  and radius  $R_{WD} \sim 3 \times 10^8$  cm, the spin-down timescale of J2211+1136 ( $P_{WD} \sim 70.32$  s and  $B_{WD} \sim 1.5 \times 10^7$  G) becomes  $\tau_{sd} \sim 200$  Gyr, which is longer than the cooling timescale. We can also see that the spin-down timescales due to the dipole radiation of J1901+1458 and ( $> 10$  Gyr) and of PG 1031+234 ( $> 100$  Gyr) are also longer than their cooling timescales. Although the true ages of the WDs are unknown, the effect of the dipole radiation is not primary mechanism for achieving the observed spin periods. This suggests that (i) those three WDs were produced with the current spin angular momentum, or (ii) a spin-down torque by other processes has operated.

The spin evolution of the merger product has been discussed by previous studies. In the models discussed in Külebi et al. (2013) and Sousa et al. (2022), for example, the main cause of the spin-down of the merger product is an interaction of the magnetic field of the product with a debris disk, which is remnant of the disrupted WD (Shen et al. 2012; Ji et al. 2013). Külebi et al. (2013) apply their model to the three magnetic WDs (WDs 0325-857, 1015+014 and PG 1031+234) with a spin period of  $\sim 10 - 200$  min and they suggest that the current spin periods are close to the values when the accretion was switched off in a timescale of  $\sim 10^4 - 5$  years. On the other hand, Shen et al. (2012) study the long-term evolution of the remnant of the DWD merger and suggest that the magnetic stress redistributes the angular momentum from the core to the Keplerian disk and quickly

establishes a rigidly rotating and giant-star-like object, which is not surrounded by the accretion disk (Schwab et al. 2012; Schwab 2021). Schwab (2021) estimates a loss of the angular momentum during the giant phase, which is supposed to last of the order of  $10^4$  years after the merger event, and predicts that the new born WD has an initial period of 10 – 20 minutes.

In this paper, we revisit the effect of the stellar wind on the spin evolution of the hot product born after the DWD merger, since the previous studies have not investigated this effect well. In particular, we will determine the position of the slow-point and the mass-loss rate of the stellar wind by solving the structure of the merger product under the assumption of the hydrostatic equilibrium. In section 2, we introduce our model for the magnetized wind and structure of the merger product. We discuss the condition of the launch of the wind and the angular momentum loss by the wind. In section 3, we discuss the general picture of the spin-down of the merger product by the magnetized wind and apply our model to the three WDs, J1901+1458, J2211+1136 and PG 1031+234, as representative examples. We compare our model with the previous studies in section 4 and summarize our results in section 5.

We note that the merger product may not be considered as a conventional WD in its initial evolution stage, because the envelope with a mass of  $M_{env} \sim 0.1 - 0.3 M_{\odot}$  is sustained by the gas and/or radiation pressures, and it may have a radius of  $> 10^{10}$  cm. However, we use the subscript “WD” to represent the physical quantities of the merger product, since the remnant eventually evolves to a WD after cooling down sufficiently.

## 2 THEORETICAL MODEL

### 2.1 Magnetohydrodynamic wind and angular momentum loss

We assume that a DWD merger creates a rapidly spinning and highly magnetized object. It has been predicted that initial stage of the merger product is very hot and produces a radiation luminosity of the order of the Eddington value (Shen et al. 2012; Schwab et al. 2016; Wu et al. 2022). Such a hot merger product may launch a magneto-hydrodynamics (MHD) wind that carries away the angular momentum of the magnetized object. An exact treatment of the MHD wind is a complicated physical process and requires a treatment of the numerical simulation (Kashiyama et al. 2019; Zhong et al. 2024). In our study, therefore, we simplify the treatment of the stellar wind to investigate a basic picture of the spin evolution of the merger product if the MHD wind would be launched. We explore a steady wind, since the spin-down timescale under the effect of the wind is in general longer than the dynamical timescale of the wind, which may be defined by  $R_A/V_A$  with  $R_A$  being the radius of the Alfvén point and  $V_A$  the wind speed at the Alfvén point. We assume that the magnetic field is a mono-pole type structure in the poloidal plane, and discuss the wind solution in the equatorial plane. Such a wind solution is greatly discussed in previous studies of the general stellar wind (Weber & Davis 1967; ?; Lamers & Cassinelli 1999; Mestel 2012). In the non-relativistic MHD wind, the equation of motion in the radial direction ( $r$ ) may be described as

$$V_r \frac{dV_r}{dr} + \frac{1}{\rho} \frac{dP_i}{dr} + \frac{Gm}{r^2} - \frac{\kappa L}{4\pi r^2 c} - \frac{V_{\phi}^2}{r} + \frac{B_{\phi}}{4\pi \rho r} \frac{d}{dr} (r B_{\phi}) = 0, \quad (3)$$

where  $m$  is the stellar mass within the radius  $r$  and  $L$  is the radiation luminosity at the radial distance  $r$ . In addition,  $V_r$  and  $V_{\phi}$  are the radial and azimuth speeds of the wind respectively,  $P_i$  is the gas pressure,  $\rho$  is the mass density of the wind,  $\kappa$  is the opacity, and  $B_{\phi}$

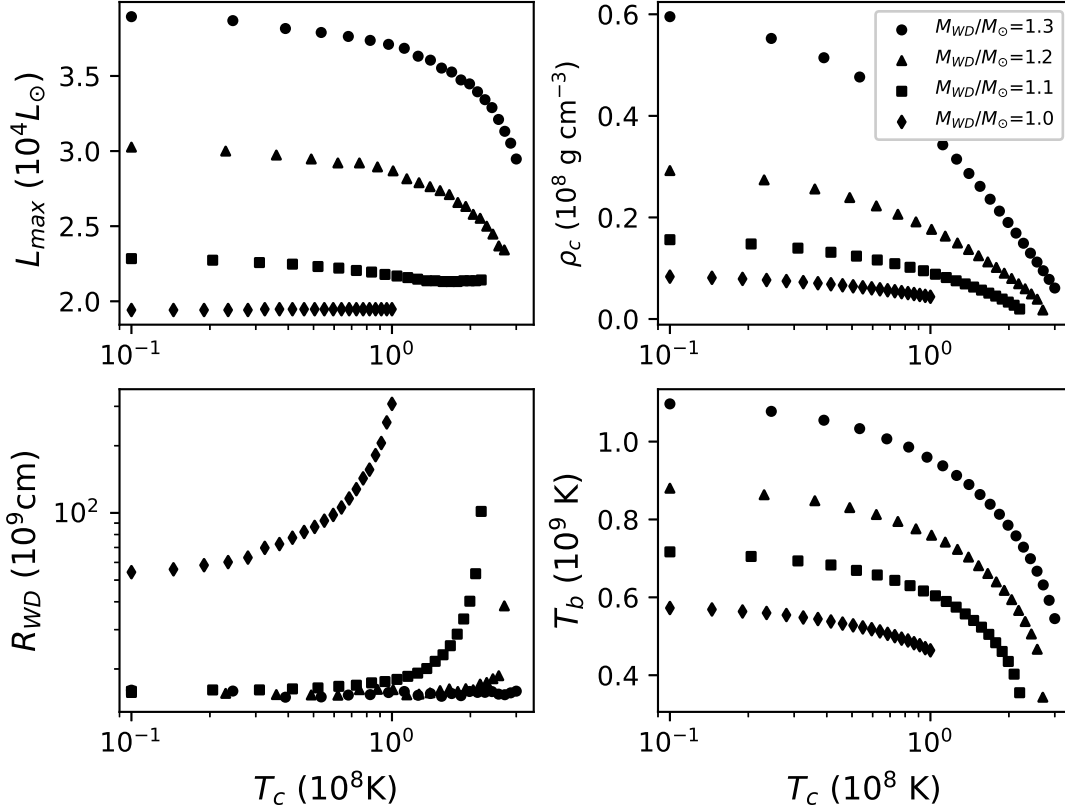


**Figure 1.** Properties of the merger product with  $L_{WD} \sim L_{max}$  as a function of the core temperature. Top-left: The luminosity above which the energy transfer via the convection may be important in the envelope. Our current calculation cannot be applicable to  $L_{WD} \geq L_{max}$ . Top-right: Central density. Bottom-left: Radius of the merger product. Bottom-right: Temperature at the core/envelop boundary. The circle, triangle, square and diamond symbols show the cases for the mass  $M_{WD}/M_\odot = 1.3, 1.2, 1.1$  and  $1.0$ , respectively. The results are envelope mass of  $M_{env} = 0.3M_\odot$  for all cases.

is the azimuthal component of the magnetic field. The fourth term on the left hand side corresponds to the radiation pressure. A steady MHD wind passes through the slow-, Alfvén- and fast-points, and it can be launched when the envelope of the merger product satisfies the condition of the slow-point. To identify the slow-point, we may rewrite the equation (3) in a form of (Kashiyama et al. 2019),

$$\left( V_r^2 - c_s^2 - \frac{A_\phi^2 V_r^2}{V_r^2 - A_r^2} \right) \times \frac{r}{V_r} \frac{dV_r}{dr} = \frac{\kappa L}{4\pi r c} + \frac{k_B}{\mu m_p} \left( -r \frac{dT}{dr} + 2T \right) - \frac{Gm}{r} + V_\phi^2 + 2V_r V_\phi \frac{A_r A_\phi}{V_r^2 - A_r^2}, \quad (4)$$

where  $T$  is the temperature,  $c_s = \sqrt{k_B T / (\mu m_p)}$  is the sound speed of the ideal gas with  $k_B$  being the Boltzmann constant,  $\mu$  the mean atomic weight and  $m_p$  the proton mass. In addition,  $A_r$  and  $A_\phi$  are local Alfvén speeds corresponding to the radial and azimuthal magnetic fields, respectively. We anticipate that at the slow-point, the Alfvén speed is much slower than the sound speed,  $A_{r,\phi} \ll c_s$ , and the rotation velocity of the wind is nearly corotation speed ( $V_\phi = 2\pi r / P_{WD}$ ). Applying these approximations on the equation (4), the condition of the slow-point may be described as (Lamers & Cassinelli 1999),

$$F(r) \equiv \frac{\kappa L}{4\pi r c} + \frac{k_B}{\mu m_p} \left( -r \frac{dT}{dr} + 2T \right) - \frac{Gm}{r} + r^2 \Omega_{WD}^2, \quad (5)$$

and

$$F(R_s) = 0 \text{ and } V_r(R_s) = c_s(R_s) \quad (6)$$

where  $R_s$  represents the radial distance to the slow-point and  $\Omega_{WD} = 2\pi / P_{WD}$  is the angular speed of the WD's spin. We evaluate the mass-loss rate of the wind at the slow-point as

$$\dot{M}_W = 4\pi R_s^2 \rho(R_s) c_s(R_s). \quad (7)$$

The angular momentum carried by the MHD wind is determined at the Alfvén-point. The rate of the angular momentum loss per unit time due to the wind may be expressed by (Mestel 1999)

$$j_w = \frac{3\dot{M}_W c^2}{2\Omega_{WD}} \left( \frac{V_M}{V_f} + \frac{V_M^3}{c^2 V_f} - 1 \right), \quad (8)$$

where  $V_M = (\Phi_B^2 \Omega_{WD}^2 / \dot{M}_W)^{1/3}$  is the so-called Michel speed,  $\Phi_B = r^2 B_r = \text{constant}$  is the radial magnetic flux, and  $V_f = c\sigma^{1/3}(1 + \sigma^{2/3})^{-1/2}$  with  $\sigma = V_M^3 / c^3$  is the terminal wind speed. In the limit of  $\sigma \ll 1$ , the equation (8) becomes  $j_w \sim \dot{M}_W V_M^2 / \Omega_{WD}$  of the non-relativistic case. The distance to the Alfvén-point may be approximately represented as  $R_A = (c/\Omega_{WD}) \{ (3\Omega_{WD} j_w / 2\dot{M}_W c^2) / [1 + (3\Omega_{WD} j_w / 2\dot{M}_W c^2)] \}^{1/2}$ , which is  $R_A \sim \sqrt{3}/2 V_M / \Omega_{WD}$  in the non-relativistic wind regime and  $R_A = c/\Omega_{WD}$  in the relativistic wind regime. The Alfvén speed

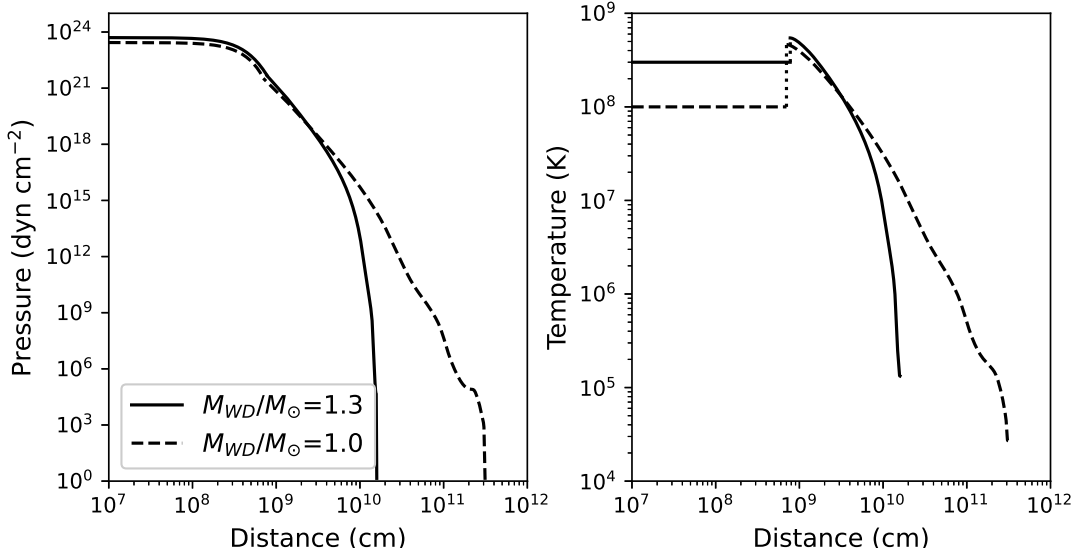


**Figure 2.** Profiles of the pressure (left panel) and temperature (right panel) for the merger products with the mass  $M_{WD}/M_{\odot} = 1.3$  (solid line) and 1.0 (dashed line), respectively. The luminosity and core temperature are  $L_{WD} = 3 \times 10^4 L_{\odot}$  and  $T_c = 3 \times 10^8$  K, respectively, for  $M_{WD}/M_{\odot} = 1.3$  and  $1.9 \times 10^4 L_{\odot}$  and  $T_c = 10^8$  K, respectively, for  $M_{WD}/M_{\odot} = 1.0$ . The envelope mass is  $M_{env} = 0.3 M_{\odot}$ .

at the Alfvén radius is expressed as  $(V_A/c) = \gamma_c / \sqrt{1 + \gamma_c^2}$  with  $\gamma_c = \gamma_A V_A / c = [1 - (\Omega_c R_A / c)^2] (c / \Omega_{WD} R_A)^2 \sigma$ , which becomes  $V_A \sim (2V_M/3)$  in the non-relativistic wind and  $V_A \sim 0.55 c$  in the relativistic wind.

For the case of the weakly magnetized merger product, the Alfvén-point, to which the radial distance is described by  $R_A \sim \sqrt{3/2} V_M / \Omega_{WD} \propto \Phi_B^{2/3}$ , may be located inside the slow-point, and the angular momentum loss by equation (8) will not be applicable. In such a situation, we anticipate that the torque from the stellar wind exerts on the stellar surface and we calculate the angular momentum loss from

$$\dot{J}_W = \frac{3}{2} \dot{M}_W R_{WD}^2 \Omega_{WD}.$$

The treatment of the MHD wind becomes inapplicable once the mass-loss rate falls to value, with which the number density at the Alfvén-point becomes of the order of the Goldreich-Julian number density of  $n_{GJ}(R_A) \sim B(R_A) \Omega_{WD} / 2\pi c e$  (Goldreich & Julian 1969). Such a lower density magnetosphere will induce a large electric field due to the rotation of the magnetized star, and may finally establish a charge-separated force-free structure. The mass-loss rate at the boundary between the two states of the magnetosphere will be of the order of  $\dot{M}_W \sim 4 \times 10^{10} (\Phi_B / 10^{26} \text{ G cm}^2) (P_{WD} / 100 \text{ s})^{-1} \text{ g s}^{-1}$ . As discussed in section 3.3, on the other hand, we will find that the typical mass-loss rate from the merger product is of the order of  $\dot{M}_W \sim 10^{20-21} \text{ g s}^{-1}$ , suggesting that the treatment of the MHD wind is applicable for the current study.

## 2.2 Structure of merger product

### 2.2.1 Assumption and approximation

Previous studies have suggested that the product after the merger is composed of a cooler core surrounded by a hotter envelope (Dan et al. 2014; Schwab et al. 2016; Schwab 2021; Wu et al. 2022). The cooler

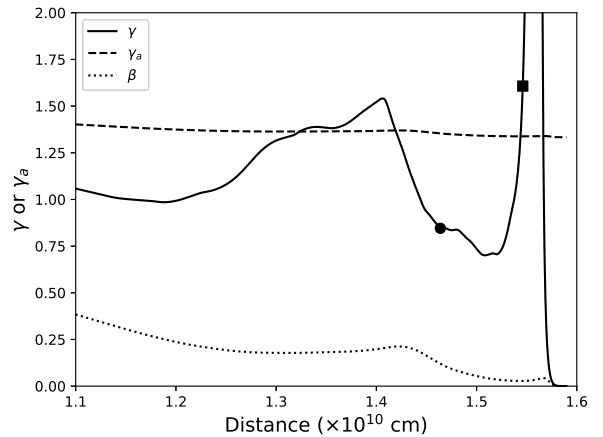


**Figure 3.** Examining Schwarzschild criterion of the convection in the envelope. The results are the structure of  $M_{WD} = 1.3 M_{\odot}$  in Figures 2. The solid line is the index defined by  $\gamma \equiv (\rho/P) |dP/d\rho|_{star}$  and the dashed line is the adiabatic index calculated from equation (21). The dotted line represents  $\beta = P_i/P$ . The filled circle and square represent the position of the slow-point and the photosphere, respectively.

core is remnant of the primary WD before the merger, and the hot envelope is mainly originated from the disrupted WD. The hot envelope can produce a radiation luminosity of the order of the Eddington value and can expand to a radius of  $r > 10^{10}$  cm, which is so-called giant phase of the merger product. In this study, we will evaluate the spin-down as a result of the MHD wind from the giant-star-like merger product.

To launch the MHD wind, the solution of the MHD equations must satisfy the condition (6) in the envelope of the merger product. It is discussed that the structure of the subsonic region ( $r < R_S$ ) is mainly determined by the hydrostatic structure, because the dynamic

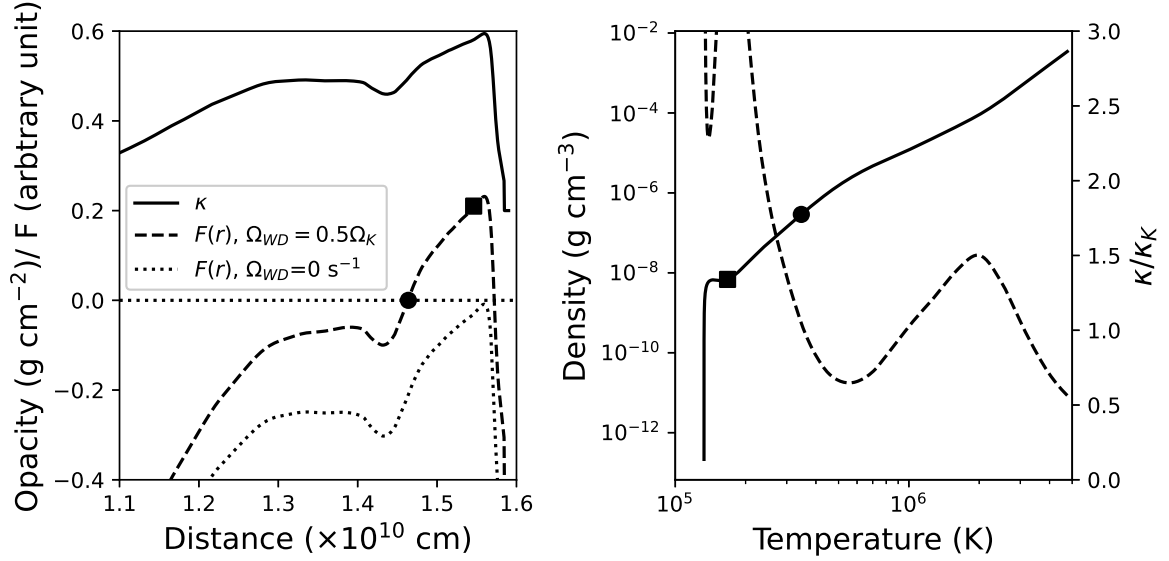


**Figure 4.** Left: Profile of the opacity (solid line) and the function  $F$  of equation (5) with the angular frequency of  $\Omega_{WD} = 0.5\Omega_K$  (dashed line) or no rotation (dotted line). The point satisfying both  $F(r) = 0$  and  $dF(r)/dr > 0$  is identified as the slow-point (filled circle). The filled square presents the position of the photosphere. The result is the case for the mass  $M_{WD} = 1.3M_{\odot}$  with the parameters same as those in Figure 2. Right: Relation between mass density and temperature (solid line) within radial distance corresponding to the left panel. The dashed line is  $\kappa/\kappa_K$ , where  $\kappa$  is the opacity defined by equation (11) and  $\kappa_K$  is the Kramer formula defined by equation (23).

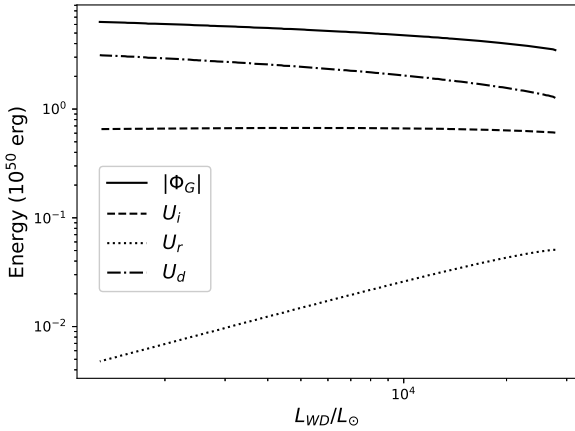


**Figure 5.** Energy of the merger product as a function of the radiation luminosity. The solid line is the absolute value of the gravitational potential energy,  $|\Phi_G|$ . The dashed, dotted and dashed-dotted lines represent the internal energies of the ideal gas ( $U_i$ ), the radiation ( $U_r$ ) and degenerate gas ( $U_d$ ), respectively. The results are case for the stellar mass of  $M_{WD}/M_{\odot} = 1.3$  and the envelope mass of  $M_{env} = 0.3M_{\odot}$ .

pressure is smaller than gas/radiation pressure (see figure 3.2 in Lamers & Cassinelli (1999)). In this study, therefore, we identify the slow-point by solving the hydrostatic structure of the non-rotating star. The effect of the stellar spin on the structure of the envelope will become an important factor when the stellar angular speed is of the order of the Keplerian value,

$$\Omega_K \equiv \left( \frac{GM_{WD}}{R_{WD}^3} \right)^{1/2}. \quad (9)$$

Nevertheless, we do not taken into account the effect of the spin for simplicity. Since the merger product is quickly spun down once the wind is launched, the final spin period, at which the condition of the slow-point is unsatisfied in the envelope, can be significantly smaller than the Keplerian value.

As presented in section 2.2.2, we will solve the hydrostatic structure of the star for the specific radiation luminosity ( $L_{WD}$ ) under the treatment of the radiative energy transfer. As the assumed luminosity increases, the outer radius of the envelop also increases. On the other hand, if the heat flux is very large, the calculated gas pressure ( $P_i$ ) at some region of the envelope increases with the radial distance, namely  $dP_i/dr > 0$ . In such a case, the assumption of the radiative energy transfer will be violated, and the convection process will describe the heat transfer. Since treatment of the convection process is complex, we restrict the radiation luminosity of  $L_{WD} < L_{max}$ , where  $L_{max}$  is the critical luminosity above which the treatment of the radiative energy transfer is violated. The critical luminosity is of the order of the Eddington luminosity of

$$L_{max} \sim \frac{4\pi GM_{WD}c}{\kappa_{max}}, \quad (10)$$

where  $\kappa_{max}$  is the maximum value of the opacity in the envelope. In section 3.1, we will evaluate the stability against convection using the Schwarzschild criterion.

The structure of the envelope depends on the main compositions through the opacity,  $\kappa$ . In this study, we will consider the main composition of the merger product is a mixture of the Carbon (C) and Oxygen (O), and calculate the opacity from

$$\kappa = \frac{\kappa_{con}\kappa_{rad}}{\kappa_{con} + \kappa_{rad}}, \quad (11)$$

where  $\kappa_{con}$  and  $\kappa_{rad}$  correspond to the conductive and radiative

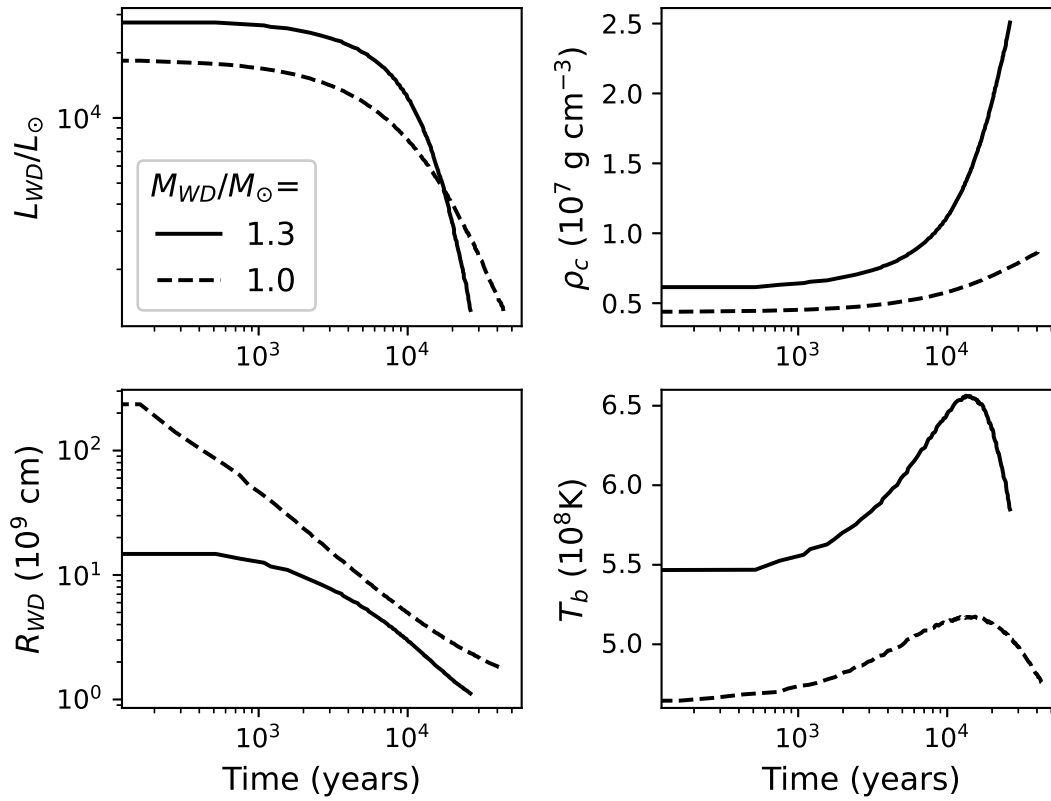


**Figure 6.** The properties of the merger product as a function of the cooling age. Top-left: Luminosity. Top-right: Central mass density. Bottom-left: Radius of the merger product. Bottom-right: Temperature at the core/envelope boundary. The solid and dashed lines are the results for  $M_{WD} = 1.3M_{\odot}$  with  $T_c = 3 \times 10^8$  K and  $1.0M_{\odot}$  with  $10^8$  K, respectively. The mass of the envelope is  $M_{env} = 0.3M_{\odot}$ .

opacities, respectively. We use the conductive opacity<sup>1</sup> presented in Cassisi et al. (2007) and ?. For the radiative opacity, we use the open code<sup>2</sup> for OPAL stellar opacity (Iglesias & Rogers 1996). We use the OPAL table for the enhanced C and O elements and apply  $X_C \sim 0.5$  and  $X_O \sim 0.5$ , respectively.

It has been suggested that the core of the primary is compressed during the merger process and its temperature can reach to  $T_c \sim (1 - 3) \times 10^8$  K (Fenn et al. 2016). However, since it has not been well investigated how the core temperature after the merger depends on the composition and mass, the previous studies assume the core temperature of  $T_c = 10^{7-8}$  K. In this study, we also treat the core temperature as a model parameter.

Inside the merger product, the temperature reaches the peak value at the region around the core/envelope boundary, as demonstrated in, for example, Schwab (2021) and Wu et al. (2022). Such a temperature profile will cause a heat transfer from the hotter envelope to the cooler core. In the current calculation of the stellar structure, however, we ignore such a heat transfer, for simplicity of the calculation. This would be reasonable approximation because the timescale of radiative transfer is of the order of  $\tau_r \sim R_c^2 \rho_c \kappa / c \sim 10^5 (R_c/3 \times 10^8 \text{ cm})^2 (\rho_c/10^8 \text{ g cm}^{-3}) (\kappa/10^{-2} \text{ cm}^2 \text{ g}^{-1})$  years, which is longer

than the spin-down timescale when the MHD wind exists and the cooling timescale with the initial radiation luminosity.

For the massive merger product ( $M_{WD} > 1.2M_{\odot}$ ), the temperature and the mass density around the core/envelope boundary may become high enough to ignite the Carbon burning process ( $\rho > 3 \times 10^5 \text{ g cm}^{-3}$  and  $T > 8 \times 10^8$  K, respectively). This Carbon burning process can last about  $10^{3-4}$  years and may leave an ONeMg WD. Such a burning process will prolong the cooling timescale and may enhance the spin-down of the merger product due to a MHD wind. In the current study, we will mainly discuss the case in which the internal temperature does not reach to the threshold of the Carbon burning process. We will discuss the influence of the burning process on our results in section 4.1.

### 2.2.2 Hydrostatic equations

We solve the structure of the merger product under the assumption of hydrostatic equilibrium,

$$\frac{dP}{dr} = -\frac{Gm\rho}{r^2}, \quad (12)$$

with equation of stellar mass,

$$\frac{dm}{dr} = 4\pi r^2 \rho. \quad (13)$$

<sup>1</sup> <http://www.ioffe.ru/astro/conduct/>

<sup>2</sup> <https://www.cita.utoronto.ca/~boothroy/kappa.html>

and the equation of state of

$$P = P_i + P_r + P_d \quad (14)$$

where  $P_i = \rho k_B T / (\mu m_p)$  is the ideal gas law,  $P_r = aT^4/3$  is the radiation pressure,  $P_d$  is the degenerate pressure of the electron (Salpeter 1961), and  $a = 4\sigma_{SB}/c$  with  $\sigma_{SB}$  being the Stefan-Boltzmann constant. For the temperature profile, we assume a constant temperature inside the core and we apply the core temperature of  $T_c \sim 10^{7-8}$  K. For the envelope, we solve the energy transfer of

$$\frac{dT}{dr} = -\frac{3\kappa\rho L}{16\pi a c r^2 T^3}. \quad (15)$$

We assume the luminosity profile of the envelope as

$$\frac{dL}{dM} = \text{constant}, \quad (16)$$

with the condition that  $L(M_{WD}) = L_{WD}$ . We ignore the radiation luminosity from the core, which with  $T_c \sim 10^8$  K will be much smaller than  $\sim 10^{37-38}$  erg s<sup>-1</sup> of the hot envelope.

### 2.2.3 Boundary condition and solving procedure

The model parameters to obtain a structure is the core temperature ( $T_c$ ), stellar mass ( $M_{WD}$ ), envelope mass ( $M_{env}$ ) and stellar luminosity ( $L_{WD}$ ). For the mass, we impose the condition that

$$m(0) = 0 \text{ and } m(R_{WD}) = M_{WD}, \quad (17)$$

at the centre ( $r = 0$ ) and the outer boundary ( $r = R_{WD}$ ), respectively. We set the radius of the core/envelop boundary ( $r = R_c$ ) when the stellar mass integrated from the centre is equal to the core mass,  $M_{WD} - M_{env}$ . For the radiation luminosity, we impose the conditions of

$$L(R_c) = 0 \text{ and } L(R_{WD}) = L_{WD}. \quad (18)$$

For the outer boundary, we determine the position by imposing the Eddington approximation of

$$T(R_{WD}) = \frac{1}{2}T_{eff} \text{ and } P(R_{WD}) \sim P_r(R_{WD}), \quad (19)$$

where  $T_{eff} = [L_{WD}/(4\pi\sigma_{SB}R_{WD}^2)]^{1/4}$  is the effective temperature.

The process to obtain a structure of the merger product is as follows:

(i) We assume the central density and solve the structure of the core from the centre. Then we find the radius of the core/envelope boundary, where  $m(R_c) = M_{WD} - M_{env}$ .

(ii) We assume the position of the outer boundary ( $R_{WD}$ ) of the envelope and solve the envelope structure from outer boundary to the core/envelope boundary. When the pressure does not match to the core pressure at the core/envelope boundary, we modify the position of the outer boundary.

(iii) If the assumed position of the outer boundary satisfies the pressure continuous at the core/envelop boundary, we check the total mass of the envelope,  $M_{env}$ . When the mass does not match to the desired mass of the envelop, we modify the central density of the core.

(iv) We repeat above processes until all imposed conditions are satisfied.

We evaluate the condition of the slow-point with the obtained hydrostatic structure. Once the condition of the slow-point is satisfied at the envelope, we evaluate the angular momentum loss due to the MHD wind, as described in section 2.1.

## 3 RESULTS

### 3.1 Hydrostatic structure

Figure 1 summarizes the properties of the merger product with the radiation luminosity of  $L_{WD} \sim L_{\max} \sim 4\pi c G M_{WD} / \kappa_{\max}$  and its dependence on the core temperature: critical luminosity (tot left), central mass density (tot right), radius (bottom-left), and temperature at core/envelope boundary (bottom-right). The figure also shows the dependency on the mass of the product; the envelope is assumed to be  $M_{env} = 0.3M_{\odot}$ . From top-left panel, we can see that the critical luminosity, above which the energy transfer due to the convection becomes important in the envelope, is of the order of  $L_{\max} \sim (1-4) \times 10^4 L_{\odot}$ . The figure does not display the results of  $T_c > 10^8$  K for  $M_{WD} = 1.0M_{\odot}$  and  $T_c > 2 \times 10^8$  K for  $M_{WD} = 1.1M_{\odot}$ , because the radius ( $R_{WD}$ ) exponentially increases above those central temperatures, as shown in the bottom-left panel. Figure 2 shows the profiles of the pressure (left panel) and temperature (right panel) for  $L_{WD} \sim L_{\max}$ ; the solid and dashed lines are the results for  $(M_{WD}, T_c) = (1.3M_{\odot}, 3 \times 10^8 \text{ K})$  and  $(1.0M_{\odot}, 10^8 \text{ K})$ , respectively. As we described in section 2.2.1, we ignored the heat transfer from the envelop to core regions and hence the temperature and mass density profiles have a discontinuity at the core/envelope boundary.

To examine the stability against convection in the envelope, Figure 3 evaluate the Schwarzschild criterion of the convection in the envelop for the case of  $M_{WD} = 1.3M_{\odot}$  in Figure 2. The index  $\gamma$  (solid line) and the adiabatic index  $\gamma_a$  (dashed line) are defined by

$$\gamma \equiv \frac{\rho}{P} \left( \frac{dP}{d\rho} \right)_{\text{star}}, \quad (20)$$

and

$$\gamma_a = \frac{32 - 24\beta - 3\beta^2}{24 - 21\beta}, \quad (21)$$

respectively, where  $\beta = P_i/P$  and the degenerate pressure in the outer envelope is neglected. We can see in Figure 3 that the current calculation with  $L_{WD} \sim 4\pi c G M_{WD} / \kappa_{\max} \sim 3 \times 10^4 L_{\odot}$  would predict a convection motion around  $r \sim 1.4 \times 10^{10}$  cm and  $\sim 1.55 \times 10^{10}$  cm, where  $\gamma > \gamma_a$ . However, the majority of the envelop satisfies the condition  $\gamma < \gamma_a$ , indicating the stability against convection. Hence, the current results discussed with the radiative heat transfer of equation (15) may be validated.

### 3.2 Slow-point at the envelope

As discussed in section 2.1, the stellar wind will be launched if the condition of the slow-point expressed by equation (6) is satisfied in the envelope of the merger product. The left panel of Figure 4 illustrates the profile of the opacity (solid line) and function  $F(r)$  (dashed line), which is defined by equation of (5), at the outer envelope; in the figure we assume the angular speed of  $\Omega_{WD} = 0.5\Omega_K$ . The figure shows that the condition for the slow-point, where  $F(r) = 0$ , is met at two locations, reflecting the profile of the opacity near the stellar surface. In this study, we consider that the slow-point not only satisfies  $F(R_s) = 0$  but also  $dF/dr|_{R_s} > 0$ . The latter condition may ensure that beyond the slow-point, the wind will be accelerated and the dynamics pressure comes to play an important role. For Figure 4, for example, the slow-point is located at  $R_s \sim 1.45 \times 10^{10}$  cm, where  $F(R_s) = 0$  and  $dF/dr|_{R_s} > 0$  are satisfied, simultaneously.

It will be important to note that in the current model, the slow-point in the envelope appears as a result of the effect of the spinning

of the remnant product. For instance, there is no solution satisfies the condition of the slow-point when  $\Omega_{WD} = 0$  s, as illustrated by the dotted line in the left panel of Figure 4. With the large radiation luminosity of  $L_{WD} \sim 10^4 L_\odot$ , we can see that the influence of the gas pressure on the function  $F(r)$ , which are the second term in the right hand side of equation (5), is negligible. The solid line in the right panel of Figure 4 presents the mass density - temperature relation at the outer envelope. It is found that with this profile of the mass density and temperature, the gas pressure term in equation (5) can be estimated about one or two order of magnitude smaller than the radiation pressure term. Consequently, the condition of the slow-point is approximately described as

$$\frac{\kappa L(R_s)}{4\pi R_s c} - \frac{Gm(R_s)}{R_s} + R_s^2 \Omega_{WD}^2 \sim 0. \quad (22)$$

As described in section 2.2.1, our solution of the hydrostatic structure is obtained under the condition of the stellar luminosity that  $L_{WD} < L_{\max}$ , above which the convection describes the heat transfer. This condition in the envelope is equivalent to the condition that  $\kappa L_{WD}/(4\pi r c) < GM_{WD}/r$ . In the current model, hence, if there is no influence of the spin, the function  $F(r)$  takes always a negative value,  $F(r) \leq 0$ , in the envelope, and no stellar wind is launched.

The dashed line in the right panel of Figure 4 presents the opacity at the outer envelope divided by the Kramer formula of

$$\kappa_K \sim \kappa_0 \rho T^{-7/2}, \quad (23)$$

where  $\kappa_0 \sim 4 \times 10^{25}$  in standard C.G.S. units. We can see that the ratio  $\kappa/\kappa_K$  is about unity at the outer envelope, except for near the outer boundary. This indicates that the opacity at the outer envelope is generally described by the Kramer formula of equation (23). In section 3.3, we will apply the Kramer formula to estimate the mass-loss rate of the MHD wind.

### 3.3 Cooling timescale and spin-down timescale

To investigate the temporal evolution of the merger product, we evaluate the cooling process of the merger product. When the nuclear burning process at the core/envelope boundary could be avoided, the merger product will evolve with a Kelvin-Helmholtz timescale. In the calculation, therefore, we carry out the grid calculation for the luminosity  $L_{WD}$ . For example, we prepare 200 grids for the luminosity in the range of  $10^3 L_\odot \leq L_{WD} \leq L_{\max}$ . Figure 5 show the energy component of the merger-product as a function of the radiation luminosity for the case of  $(M_{WD}, M_{env}, T_c) = (1.3M_\odot, 0.3M_\odot, 3 \times 10^8 \text{ K})$ ;  $\Phi_G$  is the gravitational potential energy,  $U_i$ ,  $U_r$  and  $U_d$  represent the internal energies of the ideal gas, radiation and degenerate gas, respectively. We evaluate the evolution timescale from

$$\Delta t_i = \frac{|\Delta\Phi_G + \Delta U_i + \Delta U_r + \Delta U_d|}{L_{WD} + L_\nu}, \quad (24)$$

where  $L_\nu$  represents the luminosity carried by the neutrino (Itoh et al. 1989).

Figure 6 summarizes the temporal evolution of the structures of the merger product; radiation luminosity (top-left), radius (top-right), the mass density (bottom-left) and temperature (bottom-right) at the core/envelope boundary, respectively. For the parameters of  $(M_{WD}, T_c) = (1.3M_\odot, 3 \times 10^8 \text{ K})$  (solid lines) and  $(1.0M_\odot, 10^8 \text{ K})$  (dashed lines), the evolution timescale of the initial stage is of the order of  $10^3$ - $10^4$  years. As the bottom-right panel shows, the temperature at the core/envelope boundary initially increases with time as a result of the compression of the envelope. It reaches maximum temperature at  $\sim 10^4$  years. For  $M_{WD} = 1.3M_\odot$  (solid line), we find that if the

core temperature of the merger product is  $T_c \sim 3 \times 10^8 \text{ K}$ , the maximum temperature inside does not reach to the threshold,  $\sim 8 \times 10^8 \text{ K}$ , of the Carbon burning process, and it could be possible to produce a massive CO WD. For a core temperature of  $T_c < 2 \times 10^8 \text{ K}$ , on the other hand, the maximum temperature can exceed the critical temperature of the Carbon burning, as Figure 2 indicates. The structure such as the peak temperature at the core/envelope boundary is roughly consistent with the previous studies (e.g., Shen et al. 2012).

Although we numerically solve the position of the slow-point and mass-loss rate of the MHD wind, we can perform a semi-analytical investigation for them. As discussed in section 3.2, the condition of the slow-point in the current model of the merger-product can be approximated by equation (22). We define  $\omega$  to be the ratio

$$\omega \equiv \frac{\Omega_{WD}}{\Omega_K}. \quad (25)$$

As illustrated in Figure 4, the distance between the slow-point and the outer boundary is much shorter than the radius of the merger product. We therefore assume  $R_s \sim R_{WD}$ ,  $L(R_s) \sim L_{WD}$  and  $m(R_s) \sim M_{WD}$ . Using equations (22) and (25), the opacity at the slow-point is estimated as

$$\begin{aligned} \kappa(R_s) &\sim 4\pi(1-\omega^2) \frac{GM_{WD}c}{L_{WD}} \\ &\sim 0.5(1-\omega^2) \left(\frac{M_{WD}}{M_\odot}\right) \left(\frac{L_{WD}}{10^{38} \text{ erg s}^{-1}}\right)^{-1} \text{ cm}^2 \text{ g}^{-1} \end{aligned} \quad (26)$$

To estimate the mass density at the slow-point, we apply the Kramer formula of equation (23). In addition, we introduce the parameter  $f_T$ , and represent the temperature at the slow-point as  $T(R_s) = f_T T_{eff} = f_T [L_{WD}/(4\pi\sigma_{SB}R_{WD}^2)]^{1/4}$ . From Figure 4, we can see that the parameter,  $f_T$ , is a factor of several. Consequently, the mass density at the slow-point is estimated as

$$\begin{aligned} \rho(R_s) &\sim \frac{\kappa(R_s)}{\kappa_0} f_T^{7/2} T_{eff}^{7/2} \sim 5 \times 10^{-7} \left(\frac{f_T}{2}\right)^{7/2} \left(\frac{\kappa}{0.5 \text{ cm}^2 \text{ g}^{-1}}\right) \\ &\left(\frac{L_{WD}}{10^{38} \text{ erg s}^{-1}}\right)^{7/8} \left(\frac{R_{WD}}{10^{10} \text{ cm}}\right)^{-7/4} \text{ g cm}^{-3}, \end{aligned} \quad (27)$$

where we scale the parameter  $f_T$  using the typical value of our results. Inserting equation (26) into equation (27) and using equation (7), the mass-loss rate is estimated to be

$$\begin{aligned} \dot{M}_W &= 4\pi R_s^2 \rho(R_s) c_s \sim f_T^4 \frac{\kappa L_{WD}}{\kappa_0 \sigma_{SB}} \sqrt{\frac{k_B}{\mu m_p}} \\ &\sim 10^{21} (1-\omega^2) \left(\frac{f_T}{2}\right)^4 \left(\frac{M_{WD}}{M_\odot}\right) \text{ g s}^{-1}. \end{aligned} \quad (28)$$

The current model, therefore, predicts that if the MHD wind from the merger product exists, its mass-loss rate is roughly of the order of  $\dot{M}_W \sim 10^{20-21} \text{ g s}^{-1}$ . The resultant spin-down will happen with a timescale of

$$\begin{aligned} \tau_w &\sim \frac{J_{WD}}{dJ_{WD}/dt} \sim 80\omega^{1/3} \left(\frac{I}{10^{51} \text{ g cm}^2}\right) \left(\frac{M_{WD}}{M_\odot}\right)^{1/3} \left(\frac{R_{WD}}{10^{10} \text{ cm}}\right)^{-1} \\ &\times \left(\frac{\dot{M}_W}{10^{21} \text{ g s}^{-1}}\right)^{-1/3} \left(\frac{\Phi_B}{10^{25} \text{ G cm}^2}\right)^{-4/3} \text{ years}. \end{aligned} \quad (29)$$

### 3.4 Spin-down process due to MHD wind

#### 3.4.1 Temporal evolution of wind properties

Figure 7 presents an example of the properties of the MHD wind from the merger product with  $M_{WD} = 1.3M_\odot$ ,  $M_{env} = 0.3M_\odot$ ,

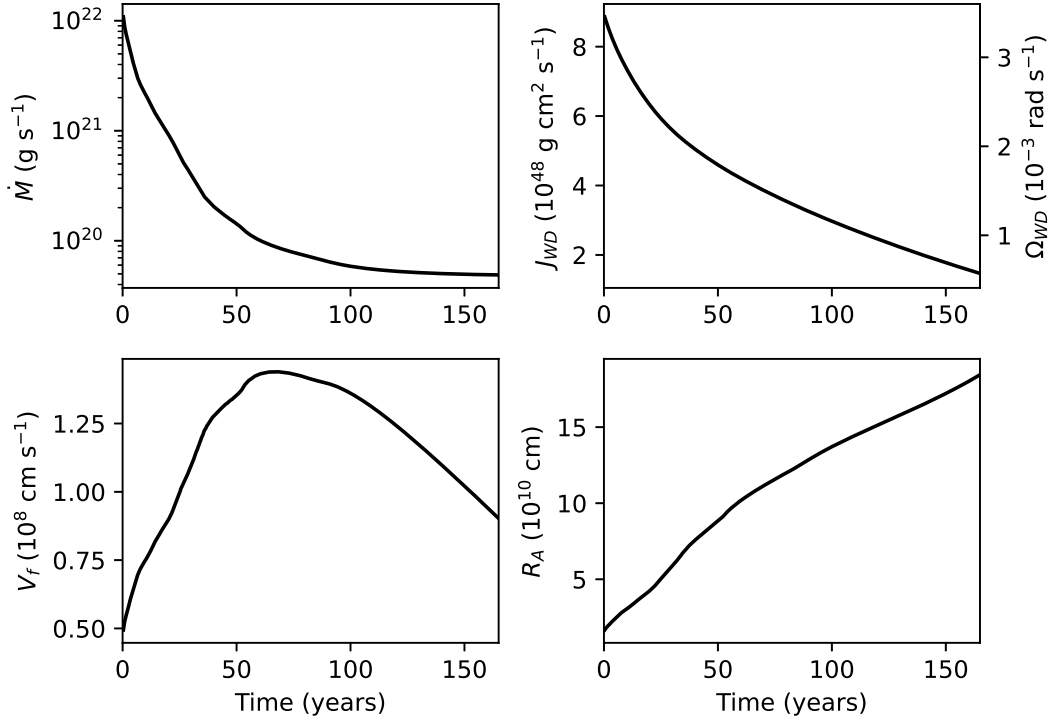


**Figure 7.** Example of the temporal evolutions of the wind properties and spin of the merger product with the mass of  $M_{WD} = 1.3M_{\odot}$ . Top-left: Wind mass-loss rate. Top-right: Angular momentum and spin frequency. Bottom-left: Terminal speed of the wind. Bottom-right: Alfvén radius. The magnetic flux is  $\Phi_B = 10^{25}\text{G cm}^2$  and the other parameters of the merger products are same as those in Figure 6.

$T_c = 3 \times 10^8$  K and the initial radiation luminosity of  $L_{WD} = 3 \times 10^4 L_{\odot}$ , for which the cooling evolution is presented in Figure 6 (solid line). We assume the initial angular speed and the magnetic flux of  $\Omega_{WD} = 0.5\Omega_K \sim 3.3 \times 10^{-3} \text{ rad s}^{-1}$  ( $J_{WD} = 8.5 \times 10^{48} \text{ g cm}^2 \text{ s}^{-1}$ ) and  $\Phi_B = 10^{25} \text{ G cm}^2$ , respectively. As shown in the figure, the angular momentum decreases with a timescale of a hundred year, which can be explained by equation of (29). The launch of the MHD wind is terminated when  $\Omega_{WD} \sim 6.4 \times 10^{-4} \text{ rad s}^{-1}$  at  $t \sim 160$  years, as top-right panel indicates.

As shown in top-left panel in Figure 7, the initial wind mass-loss rate is of the order of  $\dot{M}_W \sim 10^{22} \text{ g s}^{-1}$ , and the mass-loss rate decreases with time. The decrease in the mass-loss rate is explained as follows. The initial profile of the function  $F(r)$  is, for example, described by the dashed line in the left panel of Figure 4, in which the slow-point (filled circle) is located at  $R_s \sim 1.45 \times 10^{10} \text{ cm}$  with  $f_T \sim 2.5$ . As the spin-down timescale due to the MHD wind described by equation (29) is usually shorter than or comparable to the cooling timescale, the structure of the merger product does not significantly change during the spin-down. This indicates that as spinning down, the profile of the function  $F(r)$  in Figure 4 vertically descends toward dotted-line for the case of  $\Omega_{WD} = 0$  s, and the position of the slow-point shifts outward. This reduces the parameter  $f_T$  from 2-3 to nearly unity. Consequently, just before the wind is terminated, the mass-loss rate is of the order of  $\sim 5 \times 10^{19} \text{ g s}^{-1}$ , as indicated in the equation (28) and Figure 7.

### 3.4.2 Final angular momentum

In our model, the final angular frequency is determined as follows. As Figure 4 shows, the opacity reaches the maximum value ( $\equiv \kappa_{\max}$ ) in the envelope. From equation (22) of the condition of the slow-point, the final angular frequency is approximated by

$$\Omega_f \sim \Omega_K \left( 1 - \frac{\kappa_{\max} L_{WD}}{4\pi c G M_{WD}} \right)^{1/2}. \quad (30)$$

In the case of Figure 7, for example, the initial cooling timescale ( $\sim 10^3$  years, Figure 6) is longer than the spin-down timescale. As a result, the final angular frequency (angular momentum) is determined by the initial radiation luminosity. For the case of Figure 7, when the stellar wind is terminated, the merger remnant has the angular momentum of  $J_{WD} \sim 1.6 \times 10^{48} \text{ g cm}^2 \text{ s}^{-1}$  and it is still in the giant phase with the moment of inertia of  $\sim 2.6 \times 10^{51} \text{ g cm}^2$ . During the contraction of the envelope, the angular momentum is conserved but the angular frequency increases because of the reduce of the moment of inertia. After enough cooling process, the merger remnant with  $M_{WD} = 1.3 M_{\odot}$  will become a WD with a momentum of inertial of  $\sim 4.5 \times 10^{49} \text{ g cm}^2$ , indicating the angular frequency of the WD becomes  $\Omega_{WD} \sim 0.034 \text{ rad s}^{-1}$  or spin period of  $P_{WD} \sim 185$  s if we ignore the spin-down due to the magnetic dipole radiation.

Figure 8 shows the dependency of the final angular momentum as a function of the magnetic flux; the parameters of  $M_{WD}$ ,  $M_{env}$ ,  $T_c$  and the initial radiation luminosity  $L_{WD} = 3 \times 10^4 L_{\odot}$  are the same as the cases of Figures 2-7. In the current model, we divide the spin-down evolution into three types depending on the magnetic field; (i) strongly magnetized case, (ii) mildly magnetized case and (iii)

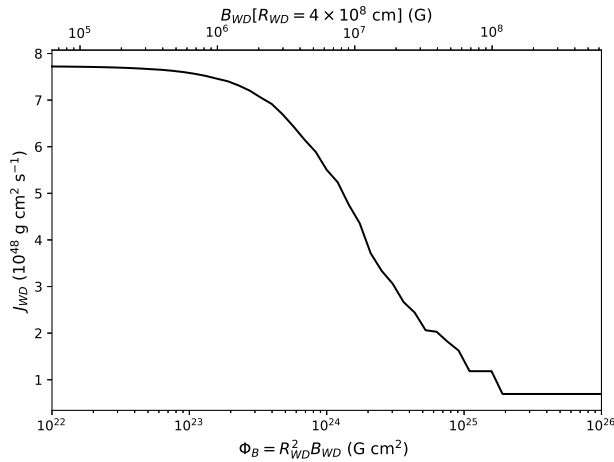


**Figure 8.** The final angular momentum when the wind is terminated, expressed as a function of the stellar magnetic flux. The expected surface magnetic field after enough cooling, for which the radius  $R_{WD} = 4 \times 10^8$  cm is used, is also indicated in upper axis. The total mass and envelope mass are  $M_{WD} = 1.3M_{\odot}$  and  $M_{env} = 0.3M_{\odot}$ , respectively. The initial luminosity and angular frequency are  $L_{WD} \sim 3 \times 10^4 L_{\odot}$  and  $\Omega = 0.5\Omega_K$ , respectively.

weakly magnetized case. For the strongly magnetized case,  $\Phi_B \geq 7 \times 10^{24}$  G cm<sup>2</sup> in Figure 8, the final angular momentum is independent on the magnitude of the magnetic field strength. This is because the initial spin-down timescale is shorter than the cooling timescale with the initial radiation luminosity. As a result, the final angular speed is approximately determined by equation (30) with the initial radiation luminosity. For the mildly magnetized case,  $10^{23}$  G cm<sup>2</sup>  $\leq \Phi_B \leq 3 \times 10^{24}$  G cm<sup>2</sup>, the initial spin-down timescale is longer than the initial cooling timescale, and the merger product can be cooled down during the MHD wind exists. The MHD wind will be terminated when the cooling timescale is comparable to the spin-down timescale. For weakly magnetized case,  $\Phi_B < 10^{23}$  G cm<sup>2</sup>, the spin-down timescale is too long and the MHD wind is ineffective to the spin-down of the merger product.

For the case that the initial angular speed and/or the initial luminosity are too small so that  $F(r) < 0$  is satisfied over envelope, no wind from the merger product is launched and no spin-down happens. In such a case, the current observed spin period of the magnetic WD will be determined by initial angular momentum or by other spin-down process. Our model also implies that when the initial luminosity is very close to  $L_{max} \sim 4\pi cGM_{WD}/\kappa_{max}$ , the MHD wind can carry away a significant fraction of the initial angular momentum and produce a slowly rotating WD (e.g. PG 1031+234).

### 3.5 Application

#### 3.5.1 J1901+1458 and J2211+1136

In this section, we apply the model to two WDs, J1901+1458 and J2211+1136, which have a current spin period of  $P_{WD} \sim 416.4$  s and  $\sim 70.32$  s, respectively, and we assume that the current angular momentum was mainly determined by the spin-down as a result of the MHD wind. Since the measured masses of J1901+1458 and J2211+1136 are  $M_{WD} \sim 1.327 - 1.365M_{\odot}$  and  $1.27M_{\odot}$ , respectively, we apply the MHD wind of the case of  $1.3M_{\odot}$ . Using the degenerate pressure of the zero temperature limit (Salpeter 1961), the moment of inertia of the WD with  $1.3M_{\odot}$  is  $I_{WD} \sim 4.5 \times 10^{49}$  g cm<sup>2</sup>, which implying current angular momenta of

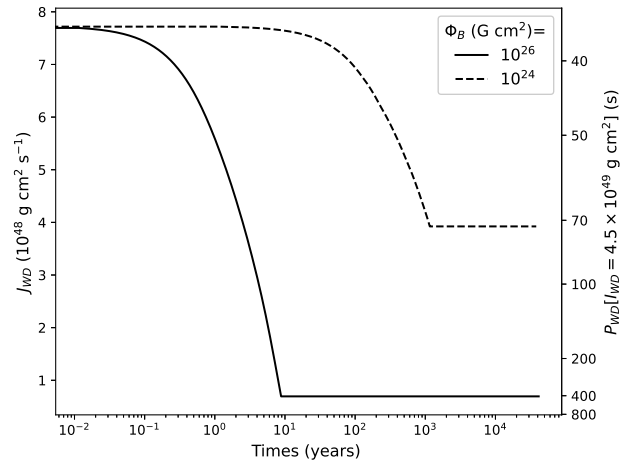


**Figure 9.** Model of the temporal evolution of the angular momentum for J1901+1458 (solid line) and J2211+1136 (dashed line). The results are for  $M_{WD} = 1.3M_{\odot}$ ,  $M_{env} = 0.3M_{\odot}$ ,  $T_c = 3 \times 10^8$  K and the initial radiation luminosity  $L_{WD} \sim 3 \times 10^4 L_{\odot}$ . The expected spin period  $P_{WD}$  once the merger remnant is sufficiently cooled down is also indicated using the right vertical axis.

J1901+1458 and J2211+1136 are  $J_{WD} \sim 6.8 \times 10^{47}$  g cm<sup>2</sup> s<sup>-1</sup> and  $4.0 \times 10^{48}$  g cm<sup>2</sup> s<sup>-1</sup>, respectively. Our model predicts that the current angular momentum has remained nearly constant after the wind ceased, as the angular momentum loss due to magnetic dipole radiation is negligible. The measured magnitudes of the magnetic field of J1901+1458 and J2211+1136 are  $B_{WD} \sim (6 - 9) \times 10^8$  G and  $\sim 1.5 \times 10^7$  G, respectively. The radius of the WD with  $M_{WD} \sim 1.3M_{\odot}$  is  $R_{WD} \sim (3 - 4) \times 10^8$  cm, suggesting J1901+1458 and J2211+1136 have a magnetic flux of the order of  $\Phi_B \sim 10^{26}$  G cm<sup>2</sup> and  $\sim 10^{24}$  G cm<sup>2</sup>, respectively.

Figure 9 shows an example of the temporal evolution of the angular momentum under the effect of the MHD wind to reach the observed values for J1901+1458 (solid line) and J2211+1136 (dashed line): the model parameters are the initial luminosity of  $L_{WD} \sim 3 \times 10^4 L_{\odot}$ , the core temperature of  $T_c = 3 \times 10^8$  K and envelope mass of  $M_{env} = 0.3M_{\odot}$ . The calculation is also taken into account the spin evolution due to the magnetic dipole radiation after the termination of the MHD wind.

As shown in the figure, the angular momenta of two cases are decreased with a timescale of  $\sim 10$  years for J1901+1458 (solid line) and  $\sim 10^3$  years for J2211+1136 (dashed line), respectively. This timescale can be explained by equation (29). For J1901+1458, the spin-down timescale with the initial angular frequency is shorter than the cooling timescale with the initial luminosity of  $L_{WD} \sim 3 \times 10^4 L_{\odot}$ . In such a case, the angular frequency when the wind is terminated is determined by equation (30) with the initial luminosity. For J2211+1136, on the other hand, the spin-down timescale is longer than the initial cooling timescale, and the spin-down process is influenced by the cooling process of the merger product. In such a case, the final angular frequency is determined by the equation (30) with the luminosity, at which the spin-down timescale is equal to the cooling timescale. After the wind is terminated, the angular momentum is almost constant with time since the timescale of the spin-down as a result of the magnetic dipole radiation (equation (2)) is much longer than the cooling timescale.

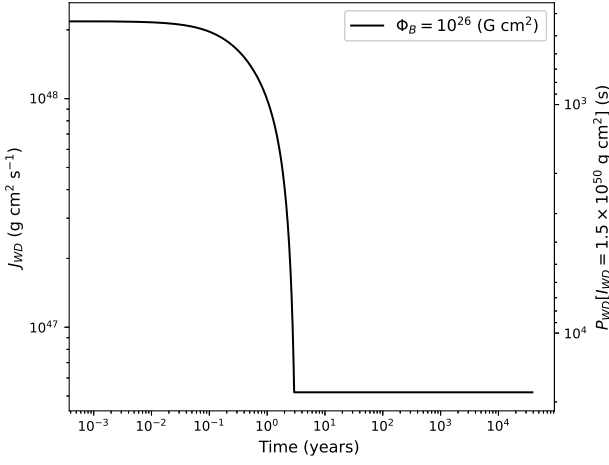


**Figure 10.** A spin-down model for PG 1031+234 with  $\Phi_B = 10^{26}$  G cm<sup>2</sup>. The parameters are  $M_{WD} = M_\odot$ ,  $M_{env} = 0.2M_{env}$ ,  $T_c = 10^8$  K, initial angular frequency  $\Omega_{WD} = 0.5\Omega_K$  and initial radiation luminosity  $L_{WD} \sim 2.2 \times 10^4 L_\odot$ . The expected spin period after the sufficiently cooling down is indicated using the right vertical axis.

### 3.5.2 PG 1031+234

PG 1031+234 is a classical magnetic WD with a magnetic field of  $B_{WD} \sim (2 - 10) \times 10^8$  G and it has a smaller mass ( $M_{WD} \sim M_\odot$ ) and a longer-spin period ( $P_{WD} \sim 212$  min) compared to those of J1901+1458 and J2211+1136. Using the degenerate pressure of the zero temperature limit, one solar mass WD has a radius of  $R_{WD} \sim 5 \times 10^8$  cm and moment of inertia of  $I_{WD} = 1.3 \times 10^{50}$  g cm<sup>2</sup>, which corresponds to the magnetic flux of  $\Phi_B \sim 10^{26}$  G cm<sup>2</sup> and current angular momentum of  $J_{WD} \sim 6.4 \times 10^{46}$  g cm<sup>2</sup> s<sup>-1</sup>. This angular momentum is significantly smaller than those of J1901+1458 and J2211+1136 discussed in section 3.5.1. Hence, if PG 1031+234 resulted from a double WD merger and its initial angular frequency was approximately Keplerian value, it experienced a stronger spin-down as a result of the MHD wind.

Figure 10 shows the model of the temporal evolution of PG 1031+234; the parameters are  $M_{WD} = M_\odot$ ,  $M_{env} = 0.2M_\odot$ ,  $T_c = 10^8$  K, initial angular frequency  $\Omega_{WD} = 0.5\Omega_K$  and initial radiation luminosity  $L_{WD} \sim 2.2 \times 10^4 L_\odot$ . Similar to J1901+1458, the initial spin-down timescale due to the MHD wind is much shorter than the cooling timescale that is in the order of  $\sim 10^3$  years. Hence the final frequency of equation (30) is determined by the initial radiation luminosity. As indicated by equation (30), when the radiation luminosity is very close to the Eddington value of  $L_{WD} \sim 4\pi cGM_{WD}/\kappa_{max}$ , which is  $\sim 2.2 \times 10^4 L_\odot$  in the current model of the stellar structure, the final angular frequency becomes significantly smaller than the Keplerian value. Our model therefore expects that PG 1031+234 appeared with the initial luminosity that is almost the Eddington value.

As indicated by the function form of equation (30), the final angular frequency is sensitive to the initial luminosity when the luminosity is close to  $L_{max}$ . Two magnetic WDs, J1901+1458 ( $P_{WD} \sim 416.4$  s) and PG 1031+234 ( $P_{WD} \sim 1.3 \times 10^4$  s), may have similar magnetic field strength ( $B_{WD} \sim (5-9) \times 10^8$  G) but appear with very different spin periods. The sensitivity of the final angular frequency on the initial luminosity would explain the difference in the spin periods of the two WDs.

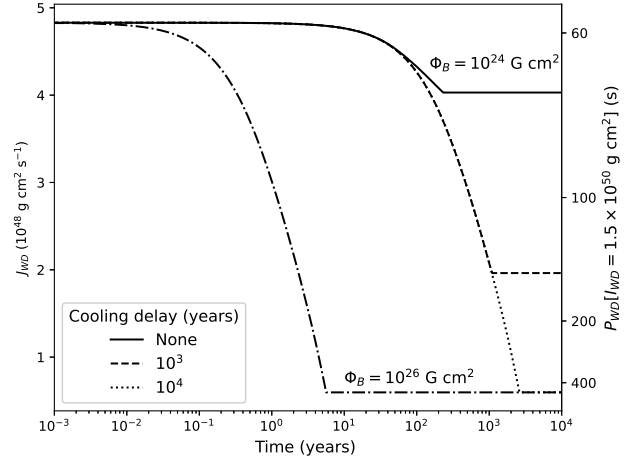


**Figure 11.** Influence of the cooling delay due to the shell-burning on the spin-down evolution. The dashed-dotted line is the case of  $\Phi_B = 10^{26}$  G cm<sup>2</sup>, for which the cooling delay does not influence the final angular momentum. The solid line is the cases for  $\Phi_B = 10^{24}$  G cm<sup>2</sup> without cooling delay, and the dashed and dotted lines are the case of a cooling delay of  $10^3$  years and  $10^4$  years, respectively. The parameters are  $M_{WD} = 1.3M_\odot$ ,  $M_{env} = 0.3M_\odot$ ,  $T_c = 2 \times 10^8$  K and initial luminosity of  $L_{WD} \sim 3.5 \times 10^4 L_\odot$ .

## 4 DISCUSSION

### 4.1 Influence on shell nuclear burning process

The temperature inside the merger product reaches the peak at the core/envelope boundary, as shown in Figure 2, and this boundary temperature depends on the core temperature, as indicated in Figure 1. During the envelope contraction phase, moreover, the boundary temperature reaches its maximum value at the age of  $t \sim 10^4$  years, as Figure 6 indicates. In section 3, we examined the stellar structure with the core temperature of  $T_c = 3 \times 10^8$  K for  $M_{WD} = 1.3M_\odot$  and  $10^8$  K for  $M_{WD} = M_\odot$ . This was because the temperature at the core/envelop boundary during the envelope contraction does not reach  $\sim 8 \times 10^8$  K of the threshold for Carbon burning process. When the core temperature for  $M_{WD} = 1.3M_\odot$  is  $T_c \leq 2 \times 10^8$  K, on the other hand, the boundary temperature will reach the threshold value and the Carbon burning will be ignited, as indicated in Figure 1. It has been argued that the Carbon shell-burning will last about  $10^3$ – $10^4$  years (Schwab et al. 2016), and this shell-burning process could delay the cooling process.

We speculate that the shell-burning process will influence the spin-down for the case that the initial spin-down timescale is longer than the initial cooling timescale when the burning process is neglected; namely, the weakly and mildly magnetized cases for  $\Phi_B < 5 \times 10^{24}$  G cm<sup>2</sup> in Figure 8. Figure 11 represents a toy model for the influence of the burning process. We assume the burning process starts from the initial stage and we artificially delay the initial cooling timescale by  $10^3$  years or  $10^4$  years with a constant radiation luminosity; we assume the core temperature of  $T_c = 2 \times 10^8$  K,  $M_{WD} = 1.3M_\odot$ ,  $M_{env} = 0.3M_\odot$  and the initial luminosity of  $L_{WD} \sim 3.5 \times 10^4 L_\odot$ , with which the boundary temperature can reach to  $T_b \sim 8 \times 10^8$  K of the threshold for Carbon burning (Figure 1).

Figure 11 indicates that for the strongly magnetized product (the dashed-dotted line), the cooling delay does not influence the final angular momentum. This is because the initial spin-down timescale is  $\sim 10$  years, which is much shorter than the cooling timescale. For the mildly magnetized case (solid, dashed and dotted lines) in the

figure, the initial spin-down timescale is of the order of  $\sim 10^3$  years, and the cooling delay can influence the final angular momentum. As indicated by the dotted-line in the figure, if the cooling delay as a result of the Carbon-burning process is longer than the spin-down timescale, the final angular momentum is determined by the luminosity during the burning process.

Figure 11 assumes that the Carbon-burning process begins at the initial stage of the evolution. It will be possible, on the other hand, that the boundary temperature is initially too low for the burning-process to start, but it reaches necessary threshold due to the envelope contraction. In such a case, onset of the burning-process will be delayed by  $10^{3-4}$  years, corresponding to the contraction timescale. We may expect that if the timescale for the onset of the burning process is longer than the spin-down timescale due to the MHD wind, the burning process does not significantly affect the spin-down evolution. Since the start time of the shell-burning process and the changes in the stellar structure and the radiation luminosity as a result of the burning process all affect the spin-down evolution, a more sophisticated model will be needed to discuss its influence on the spin-down evolution of the merger product.

## 4.2 Comparison with previous works

The evolution of the merger product has mainly been discussed with two scenarios, namely, (i) a WD surrounded by the accretion disk (Nomoto & Iben 1985; Yoon et al. 2007; Külebi et al. 2013; Sousa et al. 2022) and (ii) a giant-star-like remnant (Shen et al. 2012; Schwab et al. 2012, 2016; Wu et al. 2022). For the first scenario, a WD with a hot envelope is surrounded by an accretion disk, which is the remnant of the disrupted secondary WD, and the phase of the accretion from the Keplerian disk with an Eddington limit will continue for a timescale of  $\sim$  hours to  $\sim 10^5$  years. For the second scenario, the magnetic stress rapidly redistributes angular momentum from the core to Keplerian disk, producing a solid-rotating merger product without accompanying the accretion disk. Shen et al. (2012) argue that the timescale of the redistribution is  $\sim 10^4$  s, which is much shorter than the cooling timescale, leading the merger product to enter the giant phase. They also suggest that the rotation energy of the Keplerian disk is converted into heat and the giant-star-like object appears as a near-Eddington source.

Within the framework of the first scenario, Sousa et al. (2022) discuss the spin-evolution for J1901+1458 and J2211+1136 under the effect of the debris disk and the dipole radiation. In their calculation, the accretion rate being constant with time is assumed and the accretion from the disk continues until all initial mass of the debris disk is consumed. In their model, the observed spin periods of the magnetic WDs almost represent the equilibrium spin periods in the accretion stage, in which the co-rotation radius is equal to the Alfvén radius. Within the framework of the second scenario, we discussed the spin evolution as a result of the MHD wind, without considering the effect of the accretion disk, and applied the model to J1901+1458, J2211+1136 and PG 1031+234.

Because of the theoretical uncertainties, we may consider a potential influence of the accretion disk if it would exist in the giant phase. We assume the accretion process with an Eddington rate, which in the giant phase is of the order of

$$\begin{aligned} \dot{M}_E &= \frac{4\pi c R_{WD}}{\kappa} \\ &\sim 10^{23} \left( \frac{R_{WD}}{5 \cdot 10^{10} \text{ cm}} \right) \left( \frac{\kappa}{0.2 \text{ cm}^2 \text{ g}^{-1}} \right)^{-1} \text{ g s}^{-1}. \end{aligned} \quad (31)$$

We may express the torque exerted from the disk to the WD as

$$\dot{J}_D = \dot{M}_E R_{in}^2 \Omega_K(R_{in}) [1 - \omega(R_{in})], \quad (32)$$

where  $R_{in}$  is the distance to the edge of the disk from the center of the WD,  $\Omega_K(R_{in}) = \sqrt{(GM)/R_{in}^3}$  is the Keplerian angular speed at the inner edge and  $\omega(R_{in}) \equiv \Omega_{WD}/\Omega_K(R_{in})$  is the so-called fastness parameter. When  $\omega(R_{in}) < 1$ , namely, the edge of the disk rotates faster than the WD, the disk matter accretes on the WD's surface and spins up the WD. When  $\omega(R_{in}) > 1$ , on the other hand, the accretion system is in a propeller regime and the WD is spun down. The inner radius of the disk is determined by the equilibrium between the dynamics pressure of the disk and magnetic pressure of the WD, and it will be of the order of the Alfvén radius of the accretion system,  $R_{in} \sim \xi R_A \sim \xi [\Phi_B^2 R_{WD}^2 / (\dot{M}_E \sqrt{2GM})]^{2/7}$ , where  $\xi$  is a factor of the order of unity. We can see that with  $\dot{M}_E \sim 10^{23} \text{ g s}^{-1}$  and  $\Phi_B < 10^{26} \text{ G cm}^2$ , the aforementioned inner radius,  $R_{in}$ , is smaller than  $R_{WD}$ , indicating the torque from the disk will exert at the stellar surface,  $R_{in} \sim R_{WD}$ . The ratio of the torques from the accretion disk and from the MHD wind will be

$$\begin{aligned} \frac{\dot{J}_D}{\dot{J}_W} &\sim \frac{\dot{M}_E R_{WD}^2}{\dot{M}_W R_A^2 \omega} \sim 25 \omega^{-1} \left( \frac{\dot{M}_E}{10^{23} \text{ g s}^{-1}} \right) \\ &\times \left( \frac{\dot{M}_W}{10^{21} \text{ g s}^{-1}} \right)^{-1} \left( \frac{R_{WD}}{5 \cdot 10^{10} \text{ cm}} \right)^2 \left( \frac{R_A}{10^{11} \text{ cm}} \right)^{-2}, \end{aligned} \quad (33)$$

where  $\omega$  is given by equation (25). We find that during the accretion phase, the torque exerted from the accretion disk can be more impact on the spin evolution than that from the MHD wind. We speculate that the accretion process will keep the stellar angular frequency to be the Keplerian value, namely,  $\omega \sim 1$  and will last about  $M_{disk}/\dot{M}_E \sim 67(M_{disk}/0.1M_\odot)(\dot{M}_E/10^{23} \text{ g s}^{-1})^{-1}$  years, where  $M_{disk}$  is the initial mass of the disk. This timescale of the accretion is shorter than the cooling timescale of the merger product. After the accretion is stopped, therefore, the merger product will be spun-down by the MHD wind, as discussed in section 3.

Külebi et al. (2013) discuss the evolution of the spin due to the stellar wind, based on the scenario that a WD is surrounded by the accretion disk (the first scenario). They also discuss the effect of the launch of the MHD wind on the spin evolution by assuming that the mass-loss rate is of the order of the mass accretion rate from the disk. They suggest that the accretion process and hence MHD wind terminates once the disk temperature decreases a critical value, below which the turbulence in the disk is not sustained, and that the timescale of the disk survived is of the order of  $10^5 - 10^7$  years. They conclude that the launch of the wind enhances the spin-down of the WD.

In our scenario, the final angular momentum as a result of the MHD wind is determined by equation (30) and it depends on the initial luminosity when the merger product appears as a giant-star-like object. When the initial luminosity is  $L_{WD} \ll 4\pi c GM_{WD}/\kappa_{\max}$ , the wind will not be launched or the influence of it on the spin-down will be negligible. In such a situation, the observed periods of the magnetic WDs were determined by the initial angular momentum or by the different processes. When the merger product is appeared with the initial luminosity very close to  $L_{WD} \sim 4\pi c GM_{WD}/\kappa_{\max}$ , the MHD wind can carry away the significant fraction of the initial angular momentum. As we have discussed, our calculation of the hydrostatic equilibrium with the radiative energy transfer of equation (15) is restricted to the case of  $L_{WD} < 4\pi c GM_{WD}/\kappa_{\max}$ . Since the current model suggests that the initial radiation luminosity is an important factor to characterize the final angular momentum, a subsequent study that (i) discusses the structure of the hot envelope with

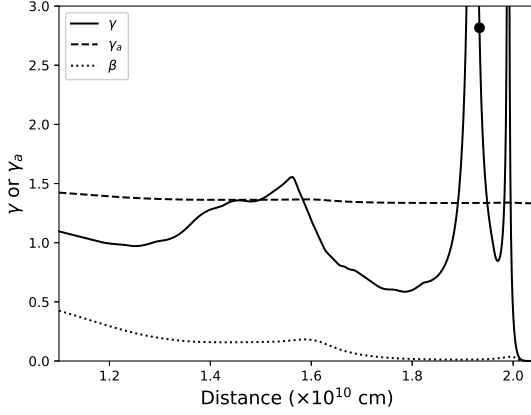


**Figure 12.** Examining Schwarzschild criterion of the convection in the envelope. The model parameters are the same as Figure 3, but the effect of the spin on the hydrostatic structure is taken into account.

the convection energy transfer and (ii) determination of the initial luminosity will be required.

### 4.3 Limitation of model

In this study, we have excluded the effects of the spin and convection motion on the stellar structures to focus on the basic picture of the spin evolution under the influence of the MHD wind. To examine the influence of the stellar spin, we may solve the hydrostatic equation of

$$\frac{dP}{dr} = -\frac{Gm\rho}{r^2} + \rho r \Omega_{WD}^2, \quad (34)$$

where the second term in the right hand side accounts for the effect of the spin. This form of the hydrostatic equation aligns more consistently with the function  $F(r)$  defined by equation (5), which was used to determine the location of the slow-point.

Figure 12 shows the profiles of the index  $\gamma = (d \log P / d \log \rho)_{\text{star}}$  (solid line) and the adiabatic index  $\gamma_a$  (dashed line) near the stellar surface. The model parameters are identical to those used in Figure 3. By comparing Figure 12 with Figure 3, we find that, as expected, the influence of the stellar spin results in an elongation of the stellar structure; the stellar radius is  $R_{WD} \sim 2 \times 10^{10}$  cm in Figure 12, while  $\sim 1.6 \times 10^{10}$  cm in Figure 3. Additionally the stellar spinning shifts the location of the slow-point (filled circle) outward, closer to the stellar surface, and results in the decrease of the mass-loss rate, as indicated by equation (28). As a result, the influence of the stellar spin would prolong the spin-down timescale of the merger product.

Figure 12 demonstrates that the slow-point is located at the convection region, where  $\gamma > \gamma_a$ . Since the convection alters the temperature profile and hence the profile of the function  $F(r)$  in the outer magnetosphere, it will also affect the location of the slow-point. Consequently, although we would expect that the basic picture of the spin-down of the merger-product is not altered, a self-consistent treatment of the coupling between the stellar spin and the stellar structure including convection will be necessary for subsequent study.

## 5 SUMMARY

The recent observations have collected evidence that the DWD merger event results in the formation of massive and magnetic WD.

In this paper, we have carried out modeling for the spin evolution of merger product that experiences a giant phase, under the influence of MHD wind. We solved the hydrostatic equilibrium of the merger product and determined the slow-point and Alfvén-point of the MHD wind. By assuming that the merger product is born with a luminosity of the order of, but less than the Eddington value, we estimate a mass-loss rate of  $\dot{M}_{\odot} \sim 10^{20-21} \text{ g s}^{-1}$  by the wind. The spin-down timescale is of the order of  $\tau_W \sim 10$  years when the magnetic flux of the merger product is  $\Phi_B \sim 10^{26} \text{ G cm}^2$  or  $\tau_W \sim 10^3$  years when  $\Phi_B \sim 10^{24} \text{ G cm}^2$ . We divided the spin-down evolution into three types depending on the magnetic flux of the merger product. For the strongly magnetized case, the initial spin-down timescale is smaller than the cooling timescale of the merger product, and the final angular momentum is approximately determined by the equation (30) with the initial luminosity. For mildly magnetized case, the merger product can be cooled down before the MHD wind is terminated. The final angular momentum is determined when the spin-down timescale is equal to the cooling timescale. For weaker magnetic case, the initial spin-down timescale is too long and the MHD wind hardly affects to the angular momentum of the merger product. We speculated that the influence of the Carbon shell-burning can be important for the mildly magnetized case, for which the spin-down timescale as a result of the MHD wind is of the order of  $10^3$  years. We applied our model to three magnetic WDs, J1901+1458, J2211+1136 and PG 1031+234. We concluded that J1901+1458 and PG 1031+234 corresponds to the strongly magnetized case, and their current spin-periods were almost determined by the initial luminosity. In contrast, J2211+1136 corresponds to a mildly magnetized case. Since the current model overlooked several physical processes, such as the heat transfer from the envelope to the core, energy transfer by the convection and the shell-burning process, further developing model will be necessary for comprehensive understanding for the spin evolution of the merger product and the variety of the spin periods of known magnetized WDs.

## ACKNOWLEDGEMENT

We thank to referee for his/her useful comments and suggestions. We acknowledge discussion with Drs S.Kisaka and Y.C. Zou and J.T. are supported by the National Key Research and Development Program of China (grant No. 2020YFC2201400) and the National Natural Science Foundation of China (grant No. 12173014).

## DATA AVAILABILITY

This is a theoretical paper, mainly analytical. All the formulas are available in the article.

## REFERENCES

- Badenes C., Maoz D., 2012, *ApJ*, **749**, L11  
 Bamba A., Terada Y., Kashiyama K., Kisaka S., Minami T., Takahashi T., 2024, *PASJ*, **76**, 702  
 Brinkworth C. S., Burleigh M. R., Marsh T. R., 2007, in Napiwotzki R., Burleigh M. R., eds, *Astronomical Society of the Pacific Conference Series Vol. 372, 15th European Workshop on White Dwarfs*. p. 183  
 Caiazzo I., et al., 2021, *Nature*, **595**, 39  
 Cassisi S., Potekhin A. Y., Pietrinferni A., Catelan M., Salaris M., 2007, *ApJ*, **661**, 1094  
 Cheng S., Cummings J. D., Ménard B., 2019, *ApJ*, **886**, 100  
 Cheng S., Cummings J. D., Ménard B., Toonen S., 2020, *ApJ*, **891**, 160

- Dan M., Rosswog S., Brüggem M., Podsiadlowski P., 2014, *MNRAS*, **438**, 14
- Fenn D., Plewa T., Gawryszczak A., 2016, *MNRAS*, **462**, 2486
- García-Berro E., et al., 2012, *ApJ*, **749**, 25
- Gentile Fusillo N. P., et al., 2021, *MNRAS*, **508**, 3877
- Goldreich P., Julian W. H., 1969, *ApJ*, **157**, 869
- Gvaramadze V. V., Gräfener G., Langer N., Maryeva O. V., Kniazev A. Y., Moskvitin A. S., Spiridonova O. I., 2019, *Nature*, **569**, 684
- Hernandez M. S., Schreiber M. R., Landstreet J. D., Bagnulo S., Parsons S. G., Chavarría M., Toloza O., Bell K. J., 2024, *MNRAS*, **528**, 6056
- Iglesias C. A., Rogers F. J., 1996, *ApJ*, **464**, 943
- Itoh N., Adachi T., Nakagawa M., Kohyama Y., Munakata H., 1989, *ApJ*, **339**, 354
- Ji S., et al., 2013, *ApJ*, **773**, 136
- Kashiyama K., Fujisawa K., Shigeyama T., 2019, *ApJ*, **887**, 39
- Kilic M., Bergeron P., Blouin S., Bédard A., 2021a, *MNRAS*, **503**, 5397
- Kilic M., Kosakowski A., Moss A. G., Bergeron P., Conly A. A., 2021b, *ApJ*, **923**, L6
- Kilic M., et al., 2023, *MNRAS*, **518**, 2341
- Koester D., Chanmugam G., 1992, in Tayler R. J., ed., *Stellar Astrophysics*, p. 77
- Korol V., et al., 2020, *A&A*, **638**, A153
- Külebi B., Ekşi K. Y., Lorén-Aguilar P., Isern J., García-Berro E., 2013, *MNRAS*, **431**, 2778
- Lamers H. J. G. L. M., Cassinelli J. P., 1999, *Introduction to Stellar Winds*
- Maoz D., Hallakoun N., 2017, *MNRAS*, **467**, 1414
- Mestel L., 1999, *Stellar magnetism*
- Mestel L., 2012, *Stellar magnetism*
- Nomoto K., Iben Jr. I., 1985, *ApJ*, **297**, 531
- Potekhin A. Y., Pons J. A., Page D., 2015, *Space Science Reviews*, **191**, 239
- Salpeter E. E., 1961, *ApJ*, **134**, 669
- Schmidt G. D., West S. C., Liebert J., Green R. F., Stockman H. S., 1986, *ApJ*, **309**, 218
- Schwab J., 2021, *ApJ*, **906**, 53
- Schwab J., Shen K. J., Quataert E., Dan M., Rosswog S., 2012, *MNRAS*, **427**, 190
- Schwab J., Quataert E., Kasen D., 2016, *MNRAS*, **463**, 3461
- Shen K. J., Bildsten L., Kasen D., Quataert E., 2012, *ApJ*, **748**, 35
- Sousa M. F., Coelho J. G., de Araujo J. C. N., Kepler S. O., Rueda J. A., 2022, *ApJ*, **941**, 28
- Temmink K. D., Toonen S., Zapartas E., Justham S., Gänsicke B. T., 2020, *A&A*, **636**, A31
- Tremblay P.-E., Bédard A., O'Brien M. W., Munday J., Elms A. K., Gentile Fusillo N. P., Sahu S., 2024, *New Astron. Rev.*, **99**, 101705
- Weber E. J., Davis Jr. L., 1967, *ApJ*, **148**, 217
- Wickramasinghe D. T., Ferrario L., 2000, *PASP*, **112**, 873
- Wu C., Xiong H., Wang X., 2022, *MNRAS*, **512**, 2972
- Yoon S. C., Podsiadlowski P., Rosswog S., 2007, *MNRAS*, **380**, 933
- Zhong Y., Kashiyama K., Takasao S., Shigeyama T., Fujisawa K., 2024, *ApJ*, **963**, 26